Journal of Science and Technology in Civil Engineering, NUCE 2020. 14 (3): 15–25

CHARACTERIZATION OF STRAIN AMPLITUDE-DEPENDENT BEHAVIOR OF HARDNESS AND INDENTATION SIZE EFFECT OF SS400 STRUCTURAL STEEL

Nguyen Ngoc Vinh[a,*], Vu Quoc Anh[b], Hong Tien Thang[a]

[a]*Department of Civil and Environmental Engineering, Sejong University, Gwangjin-gu, Seoul, South Korea*
[b]*Department of Steel and Timber Structures, Hanoi Architectural University, Km 10, Nguyen Trai road, Thanh Xuan district, Hanoi, Viet Nam*

Article history:
Received 13/03/2020, Revised 10/04/2020, Accepted 13/04/2020

Abstract

In this paper, the continuous stiffness measurement (CSM) indentation is employed to investigate fatigue mechanical properties of structural steel under cyclic loading. For this purpose, several representative analytical approaches were introduced to estimate the basic mechanical properties including Young's modulus and indentation hardness from the characteristics of the loading/unloading curves. Several experiments including CSM nanoindentation, low-cycle fatigue experiment for four strain amplitude levels, optical microscope (OM), and transmission electron microscopy (TEM) examinations were conducted to observe the variation characteristics of mechanical properties at the microscale and their micro-mechanisms. The microstructural evolution of the specimens deformed by the low-cycle fatigue was observed using the OM and TEM examinations. The standard nanoindentation experiments were then performed at different strain rate levels to characterize the influences of strain rate indentation on hardness of the material. The micro-mechanisms established based on the microstructural evolution and strain gradient plasticity theory were introduced to be responsible for the variation of indentation hardness under cyclic loading. Finally, the indentation size effect (ISE) phenomenon in SS400 structural steel was investigated and explained through the strain gradient plasticity theory regarding geometrically necessary dislocations underneath the indenter tip. The experimental results can be used for practical designs as well as for understanding the fatigue behavior of SS400 structural steel.

Keywords: cyclic loading; fatigue; nanoindentation; indentation size effect; strain rate sensitivity; structural steel.

https://doi.org/10.31814/stce.nuce2020-14(3)-02

1. Introduction

Structural steel is attributed to one of the most important materials in the construction industry. The topics regarding structural steel have also been the most studied and understood [1, 2]. The behavior of structural steel can be predicted and followed many standards and codes to define its mechanical properties, chemical compositions, the specific shape, and cross-section. These standards/codes are established by the agencies, for example, the National Institute of Standards and Technology, American Institute of Steel Construction, Korean Steel and Alloy Standard, and so on. The primary purpose

*Corresponding author. *E-mail address:* vinhnguyen@sju.ac.kr (Vinh, N. N.)

of the steel in the building industry is to construct the skeleton, which supports everything together. Structural steel is often employed as the reinforcement materials to support the materials having low tensile strength and low ductility [3, 4]. The high ductility of the structural steel is another important property, which allows redistributing the stresses in the continuous components and at the local region having high stresses. Since structural steel has energy dissipation capacity, high durability, and ductility, the structures made from structural steel have a great ability to resist dynamic loading, earthquake, and seismic loading [5–7]. Thus, this material is a good choice to construct buildings by engineers and architects. Structural steel under the effects of the operational factors in a long time can result in the embrittlement caused by corrosion damage, thermal aging, and fatigue [8]. This might lead to the reduction of material properties as well as eventually failure.

In material science, fatigue is attributed to the weakening of a material caused by the cyclic loading, leading to progressive structural damage and crack propagation [9, 10]. Historically, fatigue has been divided into two types, for example, high-cycle fatigue (number of cycle N is more than 10^4) and low-cycle fatigue (LCF), where there is significant plasticity [11, 12]. LCF has two fundamental characteristics, including low cycle phenomenon and plastic deformation in each cycle, in which the materials have finite endurance for this type of load. There is a lot of interest in investigating the influences of cyclic loading on the mechanical properties of the material, especially steel [13–20]. Srinivasan et al. [13] investigated the LCF behavior at several temperatures of 316L stainless steel. The experimental results of their research indicated that the fatigue life showed the temperature-dependent behavior, in which the fatigue life reached a maximum at the intermediate temperature range. Ye et al. [14] studied the fatigue deformation behavior of 18Cr-8Ni austenitic steel subjected to the LCF loading. The authors pointed out that the slip band spacing tended to decrease when the strain amplitude increased from 0.04% to 2%, and Vicker's hardness of all the strain amplitude levels exhibited the indentation size-dependent behavior. Mannan and Valsan [15] then studied the thermo-mechanical fatigue, creep-fatigue, and low-cycle fatigue of 9Cr-1Mo steel at high temperatures. The results from their research indicated that base metal of 316L stainless steel showed better fatigue resistance compared with weld metal at a temperature of 773 K. Ye et al. [18] applied the nondestructive indentation technique to estimate the mechanical properties in the 304L steel weld zone subjected to the LCF loading, while numerical and experimental investigation regarding the LCF behavior of P91 steel was conducted by Dundulis et al. [19].

The fracture behavior and the fatigue properties of low yielding point steel were characterized by Yang et al. [20]. The experimental results showed the excellent LCF properties, in which the number of cycles was less than 100 when the strain amplitude was more than 3%, while the number of cycles was larger than 100 with smaller strain amplitudes. Recently, Nguyen et al. [21] investigated the strain rate sensitivity behavior of structural steel subjected to the cyclic loading using the depth-sensing instrumented technique. However, the strain amplitude-dependent behavior of hardness and indentation size effect of SS400 structural steel has not been well investigated so far. Thus, a series of experiments, including nanoindentation, LCF experiments, OM, and TEM examinations were performed on the SS400 structural steel. The microstructure evolution of the specimen deformed by cyclic loading was observed using the TEM examination. The variation of indentation hardness under different strain amplitude levels was investigated using the nanoindentation experiment. Micro-mechanism was then introduced to be responsible for the variation of indentation hardness under the fatigue conditions. Finally, the indentation size effect phenomenon of SS400 structural steel was observed and analyzed.

2. Methodology

2.1. Determination of material properties from loading/unloading curves

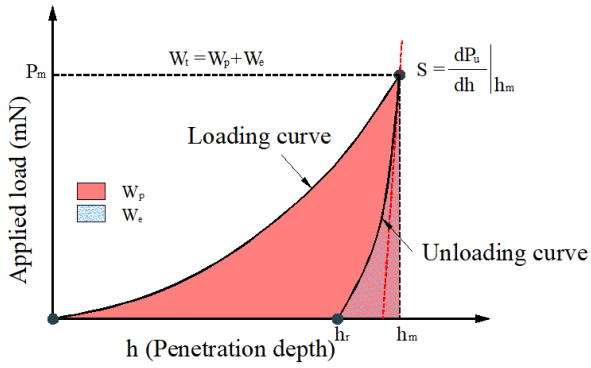

Figure 1. Indentation curve of structural steel

Fig. 1 presents the indentation curve of structural steel from the standard indentation experiment. There are several methods to extract the mechanical properties of the material from the characteristics of the indentation curves [22–24], for example, Oliver and Pharr [22]. Thus, indentation hardness (H) can be determined using Eq. (1), and elastic modulus (E) can also be estimated using Eq. (2) [25–27].

$$H = \frac{P_m}{A_c} \tag{1}$$

$$E = \left(1 - \vartheta^2\right)\left[\frac{1}{E_r} - \frac{1 - \vartheta_i^2}{E_i}\right]^{-1} \tag{2}$$

In Eq. (1), P_m and A_c are the maximum applied load and the contact area, respectively. The notation E_i and ϑ_i in Eq. (2) are the elastic modulus and Poisson's ratio of the indenter tip, and ϑ is Poisson's ratio of the tested material. The reduced modulus (E_r) is commonly calculated via the values of the contact stiffness (S) and A_c as

$$E_r = \frac{\sqrt{\pi} S}{2\beta\sqrt{A_c}} \tag{3}$$

where β is the constant factor.

2.2. Determination of strain rate sensitivity

The strain rate sensitivity is the most important parameter in the Johnson-Cook constitutive model, which is a visco-plastic model considering the temperature and strain rate influences on material behavior and fracture [28, 29]. Normally, the strain rate sensitivity of structural steel is calculated based on the results of the dynamic tensile experiment using the following equation [30]

$$m = \frac{\partial \ln\left(\sigma_y\right)}{\partial \ln(\dot{\varepsilon})} \tag{4}$$

where σ_y and $\dot{\varepsilon}$ are the yield strength and strain rate, respectively. Although the results of strain rate sensitivity from the dynamic tensile experiment are reliable, high testing cost and time-consuming

task in performing the dynamic loading tensile experiments are the limitations of this approach. Recently, nanoindentation is attributed to a promising method to determine the strain rate sensitivity of the material at the small scales, for example, microscale and nanoscale [31–34]. For the nanoindentation technique, the strain rate sensitivity is defined as the change in indentation hardness versus the change in the strain rate as

$$m = \frac{\partial \ln(H)}{\partial \ln(\dot{\varepsilon})} \tag{5}$$

2.3. Estimation of the dislocation density

Under the fatigue conditions, the dislocation structure was formed depending on the strain amplitude levels. The formation of the dislocation structure, as well as the variation of grain size subjected to the cyclic loading, was observed using the TEM and OM examinations. The dislocation density and the grain size are then calculated from TEM images. Regarding the density of the dislocations, there are two different methods to determine the dislocation density, such as X-Ray diffraction and TEM examination. To reduce the complexity of the research, the dislocation density (ρ) of the tested material can be determined from the TEM image using the following equation

$$\rho = \frac{N_{\text{Intersection}}}{A} \tag{6}$$

in which A and $N_{\text{Intersection}}$ are a tested area and the number of intersections of the dislocation lines and the surface plan. Both values of $N_{\text{Intersection}}$ and A are obtained from the TEM images.

3. Experimental procedures

The LCF experiments are performed using a universal fatigue machine (MTS fatigue testing equipment system) with the allowed capacity of 100 kN. The specimens for the LCF experiments are cut out from the steel plate with 12 mm thickness. All the LCF specimens have the same dimension, for example, 12 mm thickness, 10 mm width, and 24 mm length gauge. The geometry of the fatigue specimens is divided into three segments as follows: a clamping section, a transition section, and an effective length section. Further details of the fatigue specimens and the fatigue machine can be found out elsewhere [21]. It should be noted that the specimen preparation complies with the ASTM standard [35]. To measure the strain during fatigue testing, an electronic extensometer is employed in the center of the middle section of the specimens. A computer, which connects to the loading and measurement system, is employed to record the applied load and the number of cycles to failure. Finally, the LCF experiments are carried out at four strain amplitude (ε_a) levels, such as F-01 ($\varepsilon_a = 0.4\%$), F-02 ($\varepsilon_a = 0.6\%$), F-03 ($\varepsilon_a = 0.8\%$), and F-04 ($\varepsilon_a = 1.0\%$). It should be noted that all the fatigue experiments in this study are performed at a semi-static strain rate of 0.001 s^{-1} and a frequency of 10 Hz.

Another experiment in this study is nanoindentation. First, the specimens for nanoindentation are cut out from the middle region of the specimens deformed by the cyclic loading. Thus, the flat rectangular plates with a size of 12 mm × 10 mm × 15 mm are achieved. These specimens are mounted into the 25 mm diameter circle epoxy mold and then polished to obtain the specimen surface with high fineness as shown in Fig. 2. The standard nanoindentation experiments are performed on these polished specimens in the wide strain rate range from 0.04 s^{-1} to 0.2 s^{-1}. The same h_m of 2000 nm is used for standard nanoindentation experiments. It should be noted that an industry diamond Berkovich indenter tip with Poisson's ratio of 0.07 and an elastic modulus of 1140 GPa is employed for all

nanoindentation experiments in this study [25]. To investigate the indentation size effect of SS400 structural steel, CSM indentation experiments are also carried out in the load control mode with a maximum applied load of 190 mN, a load amplitude of 10 mN, a constant loading/unloading rate of 300 mN/min, and a frequency of 10 Hz. The preparation of specimens and performing nanoindentation experiments comply with the E2546-07 ASTM standard [36, 37]. To observe the microstructural evolution under the cyclic loading, the TEM examination is adopted. Three thin slices are cut out from the cross-section in the middle part near the fracture location. The precision ion polishing system technique is then employed to electropolish these thin slices. The TEM examinations are carried out using the TEM HF-3300 machine.

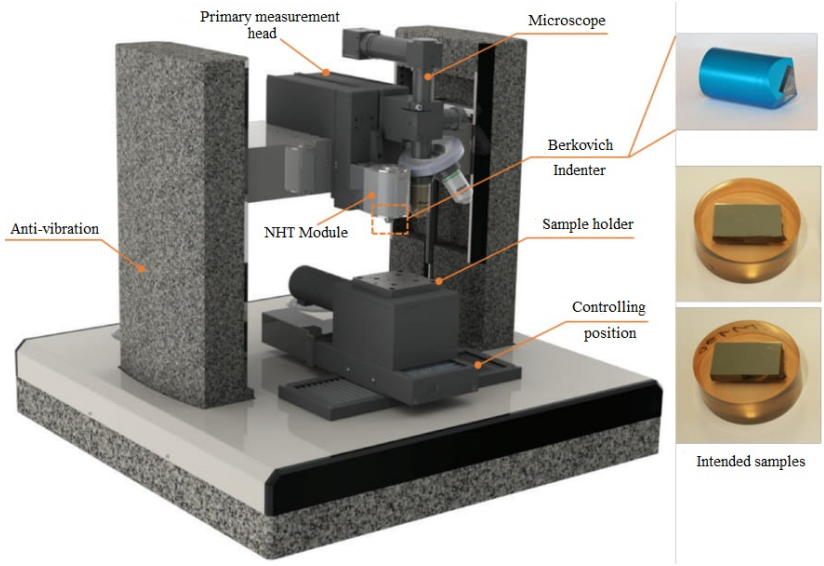

Figure 2. Nano-Hardness testing system

4. Results

4.1. Microstructural evolution under cyclic loading

Under the cyclic loading, the dislocation structure (nanostructure) strongly depends on the strain amplitude levels. Indeed, to observe the dislocation structure of the specimens deformed by the low-cycle fatigue, the TEM examination was performed, and the dislocation structure was presented in Fig. 3. It can be seen that the initial dislocation structure mainly consists of the dislocation lines with a low dislocation density. These dislocation lines are randomly arranged. At low strain amplitude (0.4%), the sub-grains and the packets of the dislocation debris were formed as shown in Fig. 3(b). The dislocations are partially developed on both the interior of the grains and the grain boundaries with randomly arranged dislocations. The sub-grains are mainly located inside the initial grains, and the individual striations can be observed in the interior of the grains. These individual striations penetrate many grains, leading to the formation of the smaller dislocation structure. At the highest strain amplitude, the progressive reduction of sub-grain size can be observed. The dislocation lines are fully developed in the interior of the grains, and higher dislocation density is also observed. The presence of the individual striations is more frequent. This might lead to the smaller size of the sub-grains, and the smaller distance of dislocation slips as observed in Fig. 3(c). Since the dislocation line

is fully developed inside the grains, it is quite difficult to distinguish the boundaries of the sub-grains. It can be deduced from the microstructural evolution that the dislocation density tends to increase with the further increase of strain amplitude, while the size of sub-grains, as well as the dislocation slip distance, show the progressive decrease as illustrated in Fig. 3.

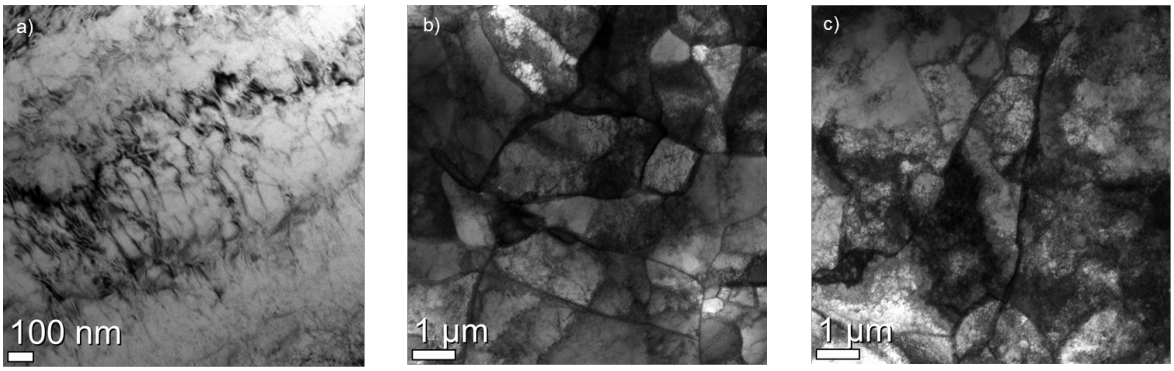

(a) The virgin specimen (b) Specimen deformed at $\varepsilon_a = 0.4\%$ (c) Specimen deformed at $\varepsilon_a = 1.0\%$

Figure 3. The evolution of dislocation structures under cyclic loading

4.2. Variation of indentation hardness

The nanoindentation experiments were then performed on the polished specimens at different strain rate from 0.04 s^{-1} to 0.2 s^{-1} for corresponding strain amplitude levels. Indentation hardness was then calculated based on the indentation parameters of the applied load-displacement curve using Eq. (1). As a result, the strain rate-indentation hardness relationship was illustrated as shown in Fig. 4.

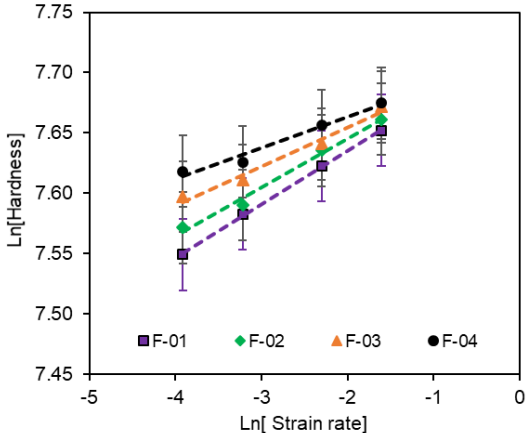

Figure 4. Variation of indentation hardness under different loading speeds

As seen, indentation hardness shows the rate-dependent behavior, in which higher indentation hardness can be observed at a higher strain rate for all cases of the strain amplitudes. Another interesting feature from Fig. 4 is that the indentation hardness depends not only on the strain rate but also on the strain amplitude. The experimental results show higher hardness for higher strain amplitude. When the strain rate increases, the effects of strain amplitude on the indentation hardness are less pronounced compared with those at a lower strain rate. Indeed, the strain amplitude strongly influences hardness at 0.04 s^{-1}, while the weak dependence of hardness on the strain amplitude can be observed at the highest strain rate as presented in Fig. 4. The hardness results are then used to calculate the strain rate sensitivity of SS400 structural steel as $m = d\ln(H)/d\ln(\dot{\epsilon})$. Therefore, the plot of logarithmic (hardness) versus logarithmic (strain rate) was established as seen in Fig. 4, and the regression analysis was then performed. Therefore, the strain rate sensitivity values of 0.026, 0.032, 0.041 and 0.045 were well determined for SS400 structural steel at the strain amplitude of 1.0%, 0.8%, 0.6%, and 0.4%, respectively.

4.3. Indentation size effect phenomenon

In the nanoindentation technique, several phenomena usually occur during the loading and unloading stages, for example, pile-up, sink-in, pop-in, indentation size effect (ISE), and so on [38–40], in which the ISE phenomenon is the decrease of hardness with increasing indentation load or increasing indentation depth [41, 42]. This ISE phenomenon can be observed in most materials, but more pronounced in the metal, especially in steel [43, 44]. This is a reason to investigate the ISE in SS400 structural steel. For this purpose, numerous CSM indentations with a sinus model were performed, and more details of the CSM experiments were presented in the previous section. The result in Fig. 5(a) shows that the ISE in SS400 structural steel is more pronounced, in which indentation hardness is very high at a shallow indent of 160 nm, quickly decreases from 5000 MPa to 2100 MPa when the indentation depth increases up to 1600 nm, and finally becomes stable at the depths over 1600 nm.

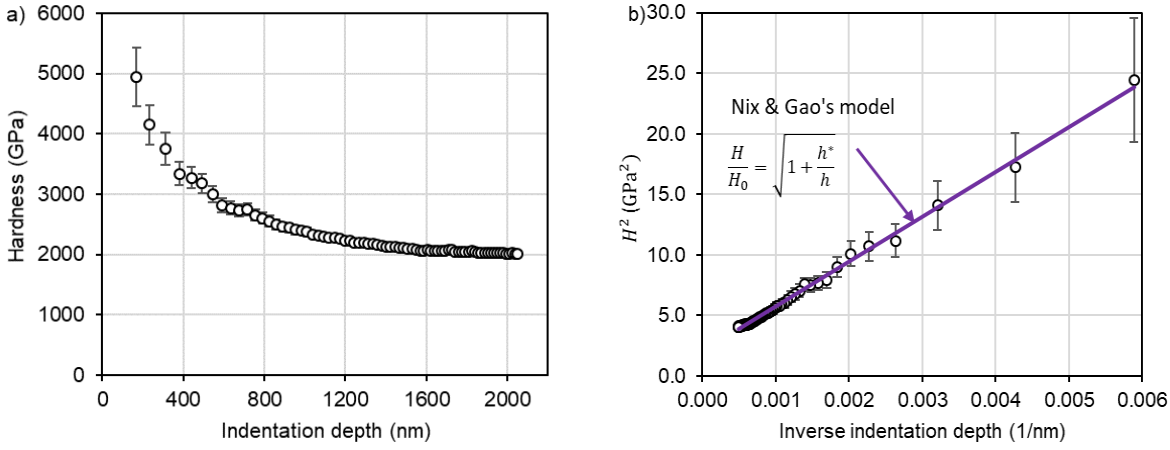

(a) Hardness-depth relationship

(b) Estimation of macro-hardness and a characteristic length using Nix & Gao model

Figure 5. Indentation size effect of SS400 structural steel

The ISE phenomenon can be explained through the strain gradient plasticity theory regarding geometrically necessary dislocation (GND). Nix and Gao [41] proposed a general model to explain the dependence of hardness on the indentation depth. This model assumes that the dislocations generated during the indentation process are stored within the hemispherical volume defined by the contact radius (a_c) as shown in Fig. 6, and the indentation hardness can be described as a function of h, macro-hardness (H_0), and a characteristic length (h^*) as

$$\frac{H}{H_0} = \sqrt{1 + \frac{h^*}{h}} \tag{7}$$

In Eq. (7), h^* can be calculated as $h^* = 40.5b\alpha^2\tan^2\theta(\mu/H_0)^2$, wherein μ, α, θ, and b are the shear modulus, a constant factor, the angle between the indenter surface and the plane of the surface, and the Burgers vector, respectively. Therefore, Nix and Gao's model was applied to interpret the experimental data in this study as shown in Fig. 5(b). As a result, H_0 of 1602.5 MPa and h^* of 1250 nm were well achieved by fitting the experimental data using Eq. (7). It can be seen that Nix and Gao's model

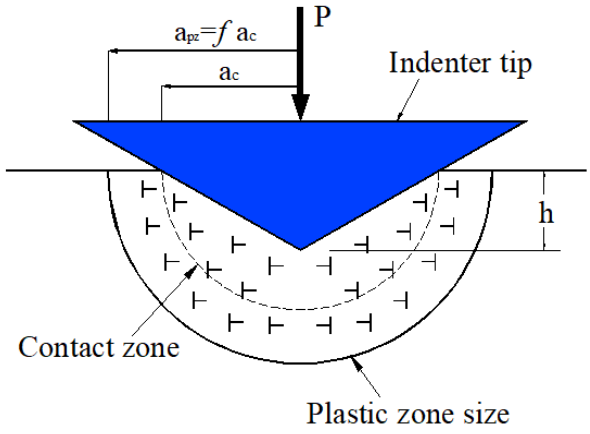

Figure 6. Schematic diagram for understanding the ISE phenomenon

describes well the depth-dependent hardness, especially for the inverse depth less than 0.002 nm^{-1}. At larger inverse depths (shallow indents), the larger standard deviation can be observed, which is caused by the blunted indenter tip, surface oxidation, and other defects [45].

5. Discussions

The behavior of indentation hardness for different strain amplitudes was observed as shown in Fig. 4. The dependence of indentation hardness on the fatigue conditions can be interpreted through the evolution of the dislocation structure and the strain gradient plasticity theory [46]. First, the relationship between the indentation hardness of the material and the dislocation density (ρ) can be described based on the strain gradient plasticity model as [41, 47]

$$H = c\sigma = c\sqrt{3}\alpha G b\sqrt{\rho} \tag{8}$$

where α and G are the constant factor and the shear modulus, respectively. In Eq. (8), c is the Tabor's factor [48]. It can be seen that indentation hardness is proportional to the square root of the dislocation density. As previously mentioned, the dislocation density showed an increase when the strain amplitude increased from 0.4% to 1.0%. Thus, it can be deduced from the evolution of the dislocation structure presented in Fig. 3 and the strain gradient plasticity theory that the dislocation density of the specimens deformed by low-cycle fatigue tends to increase with the further increase of the strain amplitude from 0.4 to 1.0%, leading to an increase of indentation hardness as observed in Fig. 4.

6. Conclusions

In this study, CSM indentation, low-cycle fatigue experiments, and TEM examination were performed to investigate the microstructural evolution, strain amplitude-dependent behavior of hardness, and indentation size effect of SS400 structural steel. The experimental and analysis results support the following conclusions:

- The dislocation density tends to increase with the further increase of the strain amplitude, while the size of sub-grains or the dislocation slip distance shows a progressive reduction.

- Indentation hardness is highly sensitive to not only strain rate indentation but also the strain amplitude level.

- The indentation size effect phenomenon is observed in SS400 structural steel. The dependence of hardness on the indentation depth is interpreted through the strain gradient plasticity theory (Nix and Gao model).

- When the strain amplitude increases from 0.4% to 1.0%, the dislocation density tends to increase, while the grain size shows a decrease, to be responsible for the strain amplitude-dependent behavior of indentation hardness in this study.

Acknowledgments

This research was supported by a grant (19CTAP-C151846-01) from the Technology Advancement Research Program (TARP) funded by the Ministry of Land, Infrastructure, and Transport of the Korean government and by a grant (2019R1A4A1021702) from the Basic Research Program through the National Research Foundation of Korea (NRF) funded by the MSIT.

References

[1] Hai, N. V., Nghiem, D. N. T., Binh, L. V., Tin, L. N. C., Cuong, N. H. (2019). Large displacement elastic analysis of planar steel frames with flexible beam-to-column connections under static loads by corotational beam-column element. *Journal of Science and Technology in Civil Engineering (STCE)-NUCE*, 13(3):85–94.

[2] Hieu, N. T., Tuan, V. A., Cuong, N. Q. (2019). Weight optimization of steel truss frames using differential evolution algorithm. *Journal of Science and Technology in Civil Engineering (STCE)-NUCE*, 13(5V): 55–64. (in Vietnamese).

[3] Viet, V. Q., Ha, H., Hoan, P. T. (2019). Evaluation of ultimate bending moment of circular concrete–filled double skin steel tubes using finite element analysis. *Journal of Science and Technology in Civil Engineering (STCE) - NUCE*, 13(1):21–32.

[4] Hieu, N. T. (2018). Simplified design method and parametric study of composite cellular beam. *Journal of Science and Technology in Civil Engineering (STCE) - NUCE*, 12(3):34–43.

[5] Thuat, D. V., Hoa, N. D., Chuong, H. V., Khanh, T. D. (2019). Single-storey industrial steel building frames with cranes designed to withstand static earthquake and wind loads. *Journal of Science and Technology in Civil Engineering (STCE) - NUCE*, 13(5V):9–19. (in Vietnamese).

[6] Thuat, D. V., Hoa, N. D., Chuong, H. V., Hung, T. V. (2019). Effects of vertical seismic actions on the responses of single-storey industrial steel building frames. *Journal of Science and Technology in Civil Engineering (STCE) - NUCE*, 13(3):73–84.

[7] Trung, N. T. (2019). Application of Hilbert Huang transform to identify the natural frequencies of steel frame. *Journal of Science and Technology in Civil Engineering (STCE) - NUCE*, 13(2):64–73.

[8] Thu, P. T. N., Tuan, P. Q. (2019). Effects of protective cover forms on behavior of I-shaped steel beams under elevated temperature. *Journal of Science and Technology in Civil Engineering (STCE) - NUCE*, 13 (5V):47–54. (in Vietnamese).

[9] Wikipedia (2018). *Fatigue (material)*. Wikipedia Free Encylopedia.

[10] Vuong, N. V., Quan, M. H. (2019). Fatigue analysis of jacket support structure for offshore wind turbines. *Journal of Science and Technology in Civil Engineering (STCE) - NUCE*, 13(1):46–59.

[11] Murakami, Y., Miller, K. J. (2005). What is fatigue damage? A view point from the observation of low cycle fatigue process. *International Journal of Fatigue*, 27(8):991–1005.

[12] Wikipedia (2019). *Low-cycle fatigue*. Wikipedia Free Encylopedia.

[13] Srinivasan, V. S., Sandhya, R., Bhanusankararao, K., Mannan, S. L., Raghavan, K. S. (1991). Effects of temperature on the low cycle fatigue behaviour of nitrogen alloyed type 316L stainless steel. *International Journal of Fatigue*, 13(6):471–478.

[14] Ye, D., Matsuoka, S., Nagashima, N., Suzuki, N. (2005). Multi-scale deformation behavior investigation of 18Cr–8Ni austenitic steel subjected to low-cycle fatigue loading. *Materials Characterization*, 55(2): 106–117.

[15] Mannan, S. L., Valsan, M. (2006). High-temperature low cycle fatigue, creep–fatigue and thermomechanical fatigue of steels and their welds. *International Journal of Mechanical Sciences*, 48(2):160–175.

[16] Ye, D., Xu, Y., Xiao, L., Cha, H. (2010). Effects of low-cycle fatigue on static mechanical properties, microstructures and fracture behavior of 304 stainless steel. *Materials Science and Engineering: A*, 527 (16-17):4092–4102.

[17] Saad, A. A., Sun, W., Hyde, T. H., Tanner, D. W. J. (2011). Cyclic softening behaviour of a P91 steel under low cycle fatigue at high temperature. *Procedia Engineering*, 10:1103–1108.

[18] Ye, D., Mi, F., Liu, J., Xu, Y., Chen, Y., Xiao, L. (2013). Use of instrumented indentation testing to study local mechanical properties of 304L SS welded joints subjected to low-cycle fatigue loadings. *Materials Science and Engineering: A*, 564:76–84.

[19] Dundulis, G., Janulionis, R., Grybėnas, A., Makarevičius, V., Dundulis, R. (2017). Numerical and experimental investigation of low cycle fatigue behaviour in P91 steel. *Engineering Failure Analysis*, 79: 285–295.

[20] Yang, L., Gao, Y., Shi, G., Wang, X., Bai, Y. (2018). Low cycle fatigue property and fracture behavior of low yield point steels. *Construction and Building Materials*, 165:688–696.

[21] Nguyen, N.-V., Pham, T.-H., Kim, S.-E. (2019). Strain rate sensitivity behavior of a structural steel during low-cycle fatigue investigated using indentation. *Materials Science and Engineering: A*, 744:490–499.

[22] Oliver, W. C., Pharr, G. M. (1992). An improved technique for determining hardness and elastic modulus using load and displacement sensing indentation experiments. *Journal of Materials Research*, 7(6):1564–1583.

[23] Pham, T.-H., Kim, J. J., Kim, S.-E. (2015). Estimating constitutive equation of structural steel using indentation. *International Journal of Mechanical Sciences*, 90:151–161.

[24] Chang, C., Xiao, G., Liu, E., Lin, J., Zhang, X., Long, X., Zhang, L.-l. (2019). Revisiting the procedure for characterising mechanical properties in welded joints through nanoindentation. *Materials Science and Technology*, 35(8):986–992.

[25] Nguyen, N.-V., Pham, T.-H., Kim, S.-E. (2018). Characterization of strain rate effects on the plastic properties of structural steel using nanoindentation. *Construction and Building Materials*, 163:305–314.

[26] Nguyen, N.-V., Pham, T.-H., Kim, S.-E. (2019). Microstructure and strain rate sensitivity behavior of SM490 structural steel weld zone investigated using indentation. *Construction and Building Materials*, 206:410–418.

[27] Hoan, P. T., Vinh, N. N., Tung, N. T. T. (2019). Indentation for investigation of strain rate effect on mechanical properties in structural steel weld zone. *Journal of Science and Technology in Civil Engineering (STCE)-NUCE*, 13(3):104–112.

[28] Murugesan, M., Jung, D. (2019). Johnson Cook Material and Failure Model Parameters Estimation of AISI-1045 Medium Carbon Steel for Metal Forming Applications. *Materials*, 12(4):609.

[29] Johnson, G. R., Cook, W. H. (1983). A constitutive model and data for metals subjected to large strains, high strain rates and high temperatures. In *Proceedings of the 7th International Symposium on Ballistics*, volume 21, The Netherlands, 541–547.

[30] Luecke, W. E., McColskey, J. D., McCowan, C. N., Banovic, S. W., Fields, R. J., Foecke, T., Siewert, T. A., Gayle, F. W. (2005). *Mechanical properties of structural steels*. National Institude of Standards and Technology, Washington.

[31] Liu, Y., Hay, J., Wang, H., Zhang, X. (2014). A new method for reliable determination of strain-rate sensitivity of low-dimensional metallic materials by using nanoindentation. *Scripta Materialia*, 77:5–8.

[32] Wei, Q. (2007). Strain rate effects in the ultrafine grain and nanocrystalline regimes—influence on some constitutive responses. *Journal of Materials Science*, 42(5):1709–1727.

[33] Nguyen, N.-V., Kim, S.-E. (2020). Experimental study to investigate microstructure and continuous strain rate sensitivity of structural steel weld zone using nanoindentation. *International Journal of Mechanical Sciences*, 174:105482.

[34] Nguyen, N.-V., Pham, T.-H., Kim, S.-E. (2019). Strain rate-dependent behaviors of mechanical properties of structural steel investigated using indentation and finite element analysis. *Mechanics of Materials*, 137: 103089.
[35] ASTM (2004). *Test method for strain-controlled fatigue testing*. E606/E606M-12, 96:1–16.
[36] ASTM E2546-07 (2007). *Standard practice for instrumented indentation testing*.
[37] ASTM-E3 (2011). *Standard guide for preparation of metallographic specimens*. ASTM Int, 1–12.
[38] Shankar, S., Loganathan, P., Mertens, A. J. (2015). Analysis of pile-up/sink-in during spherical indentation for various strain hardening levels. *Structural Engineering and Mechanics*, 53(3):429–442.
[39] Giannakopoulos, A. E., Suresh, S. (1999). Determination of elastoplastic properties by instrumented sharp indentation. *Scripta Materialia*, 40(10):1191–1198.
[40] Chen, K.-W., Jian, S.-R., Wei, P.-J., Jang, J. S.-C., Lin, J.-F. (2010). A study of the relationship between semi-circular shear bands and pop-ins induced by indentation in bulk metallic glasses. *Intermetallics*, 18 (8):1572–1578.
[41] Nix, W. D., Gao, H. (1998). Indentation size effects in crystalline materials: A law for strain gradient plasticity. *Journal of the Mechanics and Physics of Solids*, 46(3):411–425.
[42] Durst, K., Backes, B., Franke, O., Göken, M. (2006). Indentation size effect in metallic materials: Modeling strength from pop-in to macroscopic hardness using geometrically necessary dislocations. *Acta Materialia*, 54(9):2547–2555.
[43] Rodriguez, R., Gutierrez, I. (2003). Correlation between nanoindentation and tensile propertiesInfluence of the indentation size effect. *Materials Science and Engineering: A*, 361(1-2):377–384.
[44] Arthur, E. K., Ampaw, E., Kana, M. G. Z., Akinluwade, K. J., Adetunji, A. R., Adewoye, O. O., Soboyejo, W. O. (2015). Indentation size effects in pack carbo-nitrided AISI 8620 steels. *Materials Science and Engineering: A*, 644:347–357.
[45] Haghshenas, M., Khalili, A., Ranganathan, N. (2016). On room-temperature nanoindentation response of an Al–Li–Cu alloy. *Materials Science and Engineering: A*, 676:20–27.
[46] Begley, M. R., Hutchinson, J. W. (1998). The mechanics of size-dependent indentation. *Journal of the Mechanics and Physics of Solids*, 46(10):2049–2068.
[47] Durst, K., Backes, B., Göken, M. (2005). Indentation size effect in metallic materials: Correcting for the size of the plastic zone. *Scripta Materialia*, 52(11):1093–1097.
[48] Tabor, D. (1951). *The hardness of metals*. Oxford at the Clarendon Press.